Changes in the meridional overturning circulation at 32ºS in the Pacific Ocean in 2017

Cristina Arumí Planas

2019/2020

Tutor: Alonso Hernández Guerra
Cotutora: Maria Casanova Masjoan

Trabajo Fin de Título para la obtención del Máster Universitario en Oceanografía

Changes in the meridional overturning circulation at 32ºS in the Pacific Ocean in 2017

Trabajo de fin de título presentado por Cristina Arumí Planas para la obtención del título de Máster Universitario en Oceanografía por la Universidad de las Palmas de Gran Canaria, la Universidad de Vigo y la Universidad de Cádiz.

Tutor: Dr. Alonso Hernández Guerra, Instituto de Oceanografía y Cambio Global, Departamento de Física, Facultad de Ciencias del Mar, Universidad de Las Palmas de Gran Canaria.
Cotutora: Maria Casanova Masjoan, Instituto de Oceanografía y Cambio Global, Departamento de Física, Facultad de Ciencias del Mar, Universidad de Las Palmas de Gran Canaria.

Cristina Arumí Planas Alonso Hernández Guerra Maria Casanova Masjoan

Las Palmas de Gran Canaria, a 25 de junio de 2020

TABLE OF CONTENTS

ABSTRACT

The meridional circulation and transports at 32ºS in the Pacific Ocean in 2017 are compared with analogous data from 2003 and 2009. The hydrographic data come from the GO-SHIP database and an inverse box model has been applied with several constraints. The Pacific Ocean overturning circulation pattern is similar for the three years, but the intensity of the overturning in 2009 (43.6 ± 2.3 Sv) is higher than in 2003 (32.1 ± 2.2 Sv) and in 2017 (34.9 ± 2.4 Sv). The horizontal distribution of mass transports at all depths in 2017 changes notably from the "bowed gyre" found in 2009 and resembles that regular shape of 2003. Furthermore, the East Australian Current transport decreases slightly from 2003 (51.1 ± 2.0 Sv) and 2009 (-49.9 ± 2.1 Sv) to 2017 (-39.2 ± 1.6 Sv). The Peru-Chile Current transport estimated in 2017 (4.4 ± 0.8 Sv) is slightly higher than in 2003 (3.3 ± 0.9 Sv) and in 2009 (3.8 ± 1.2 Sv). The Peru-Chile Undercurrent transport estimated in 2017 (-1.5 ± 0.8 Sv) is lower than in 2003 (2.8 ± 1.2 Sv) and 2009 (3.8 ± 1.2 Sv). Nevertheless, the heat transport in 2017 (0.4 ± 0.1 PW) has the same value as in 2003 (0.4 ± 0.1 PW) and differs from 2009 (0.2 ± 0.1 PW). The freshwater transport results show an increase in net evaporation from 2003 (0.25 ± 0.02 Sv) to 2009 (0.50 ± 0.03 Sv), and a decrease in 2017 (0.34 ± 0.08 Sv).

1. INTRODUCTION

The World Ocean Circulation Experiment (WOCE) was a global oceanographic research program surveying every ocean basin with high-quality hydrographic data, from transoceanic zonal and meridional sections of closely spaced stations. This allowed the estimation of the oceanic transports of water mass, silicate, heat, freshwater and other properties from the sea surface waters to the seafloor of every ocean (Chapman, 1998; Ganachaud, 2003; Ganachaud & Wunsch, 2000, 2003; Macdonald & Wunsch, 1996). As summarized in both Gordon (1986) and Schmitz (1995), the general features of the ocean's global overturning were long predated before WOCE. However, the newly-developed approach of inverse modelling along with the newly collected data allowed an improved, internally consistent, quantification of global transports (Roemmich & Wunsch, 1985; Wunsch, 1996). From these data, a clear picture of the Meridional Overturning Circulation (MOC) is emerged, which is a variable-in-time three dimensional system based on all the ocean basins (Gordon, 1986; Lumpkin & Speer, 2007; Talley, 2003). Firstly, there is net deep inflow of dense Antarctic Bottom Water (AABW) and North Atlantic Deep Water (NADW) into the Pacific Ocean. Secondly, these waters upwell feeding the Pacific Deep Water (PDW), found in the deep layers of the

Pacific Ocean, which flows southward into the Southern Ocean. Furthermore, diapycnal upwelling also occurs up into the Antarctic Intermediate Water (AAIW) and thermocline layers, with a southward transport back to the Indian and Southern Ocean (Talley, 2013; Wijffels et al., 2001). The Indonesian Throughflow (ITF) is the main gateway of upwelled upper layer waters from the Pacific Ocean transported westward into the surface waters of the Indian Ocean (Hernández-Guerra & Talley, 2016).

According to WOCE, the following step is to estimate how the property transports and patters of circulation have changed over time. In order to accomplish this purpose, repeat hydrographic sections in key latitudes and longitudes have been carried out in the framework of the Global Ocean Ship-Based Hydrographic Investigation Program (GO-SHIP) (www.go-ship.org). Horizontal sampling of different ocean properties (including temperature, salinity, nutrients and oxygen) are collected by high accuracy measurements from the surface to the bottom of the ocean with an approximate decadal base, a spatial resolution related to the internal Rossby radius, and sections that extend from coast to coast or enclosed regions. The inverse method is used to estimate the ocean circulation and property transports from closed hydrographic sections (Wunsch, 1977, 1996). Results from the inverse model differ depending on the prior variance specified, and on specific constraints and initial conditions imposed in the model. In our case, we will use the same constraints as in Hernández-Guerra & Talley (2016) to be able to compare our results with their results.

The South Pacific subtropical gyre is the largest in the world's oceans, extending zonally approximately 40% of the way around the Earth (Wijffels et al., 2001). At 32^{o}S in the South Pacific Ocean, the boundary currents in the thermocline layers of the subtropical gyre are the East Australian Current (EAC) in the western boundary, and a set of boundary flows alternating in sign in the eastern boundary: the Peru-Chile Current and the Peru-Chile Undercurrent. The EAC is the intense western boundary current flowing along the east Australian shelf break and slope as part of the anticyclonic circulation of the south Pacific gyre (Hamon & Tranter, 1971; Tomczak & Godfrey, 1994). The presence of New Zealand, near 34^{o}S, distorts the circulation in the southern limb (Godfrey, 1989), causing the EAC to separate from the Australian coast and flows eastward, with its southern boundary forming a strongly eddying feature: the Tasman Front (Stanton, 1979). The Peru-Chile Current is the wide eastern boundary current, flowing northward along the upper waters of the west coast of South America. The Peru-Chile Undercurrent is a subsurface current flowing southward over the slope along the Peruvian and Chilean coasts (Strub et al., 1998).

The main goal of this study is to extend a previous study of the Pacific Ocean at 32ºS carried out by Hernández-Guerra & Talley (2016), as well as to estimate if the ocean circulation has changed through different decades analyzing hydrographic data collected in 2017. To accomplish these goals, section 2 presents de data and the vertical sections of the different ocean properties, aimed at describing the main water masses present at 32ºS. Section 3 describes the geostrophic transport relative to the reference level and presents the characteristics of our inverse model. The final mass and silicate transports obtained after applying the inverse model are described in section 4, including the estimate of the meridional overturning circulation and its variability. Section 5 presents the horizontal circulation focusing on the upper, deep and abyssal layers. Section 6 describes the heat and freshwater transports. Finally, section 7 gives a discussion with conclusive remarks.

2. DATA, VERTICAL SECTIONS AND WATER MASSES

Geostrophic velocity and transport are calculated using temperature-salinity profiles collected at stations along section P06 at nominally 32ºS in the Pacific Ocean in 2017 (Figure 1). The velocities at the reference level are initially estimated from Lowered Acoustic Doppler Current Profiler (LADCP) and Shipboard Acoustic Doppler Current Profiler (SADCP), and finally adjusted from an inverse box model. These data were collected as part of the international Global Ocean Ship-Based Hydrographic Investigations Programme (GO-SHIP) (Talley et al., 2016), and are available through the CLIVAR and Carbon Hydrographic Data Office (CCHDO, http://cchdo.ucsd.edu) (Table 1). The distances between stations were typically 50 km, with smaller spacing across boundary currents and across strong topographic slopes. At each station, a temperature and salinity every two decibars were collected for the full water column depth using a SeaBird 911+ Conductivity-Temperature-Depth (CTD), as well as water samples for salinity, oxygen, silicate and other chemical tracers. However, only the temperature and salinity from CTD and silicate data are used in the inverse model.

Additionally, SADCP data, collected using a 38 kHz narrowband RDI system, were used to geostrophic velocity referencing, complemented by some LADCP station profiles. For both cruises, a system formed by a downward-looking (300 kHz) and an upward-looking (150 kHz) LADCPs were used to provide a velocity profile from the surface to the bottom of the ocean at each station. As geostrophy inherently integrates the velocity between stations, LADCP velocities on station are a poor match with respect to the horizontal sampling: their average approaches the true average only to the extent

that features are well-resolved by the station spacing. While the full SADCP data set can be used to average between stations, so it matches the integration inherent in geostrophy (E. Firing, personal communication). For this reason, we expect the SADCP data to be a more useful tool for our estimation of velocity at the reference layer.

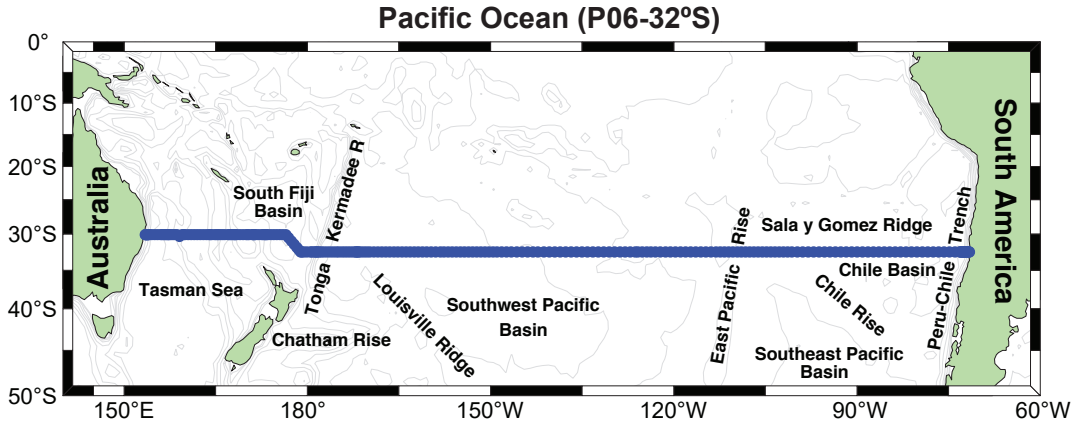

Figure 1. Station positions for P06 cruises carried out at nominally 32ºS in the Pacific Ocean in 2017.

Table 1. Hydrographic cruise information. All CTD data are available online from the CLIVAR and Carbon Hydrographic Data Office (CCHDO, http://cchdo.ucsd.edu/). LADCP and SADCP data for P06-West and P06-East are available online from the CLIVAR archive https://usgoship.ucsd.edu/cruise-data-submit-download/.

Cruise	Dates	No. stations	CCHDO Expocode	Ship	Chief scientist
P06-West	2017-07-03 to 2017-08-17	143	320620170703	Nathaniel B. Palmer	S. Mecking (Applied Physics Laboratory, University of Washington, USA)
P06-East	2017-08-20 to 2017-09-30	107	320620170820	Nathaniel B. Palmer	K. Speer (Department of Oceanography, The Florida State University, USA)

The NCEP wind stress is used to compute Ekman transports (Kalnay et al., 1996), interpolating it to the location of each station pair where the geostrophic velocity is calculated. The resulting surface winds for the cruise period is shown in figure 2 giving an Ekman transport of 0.33 ± 0.16 Sv.

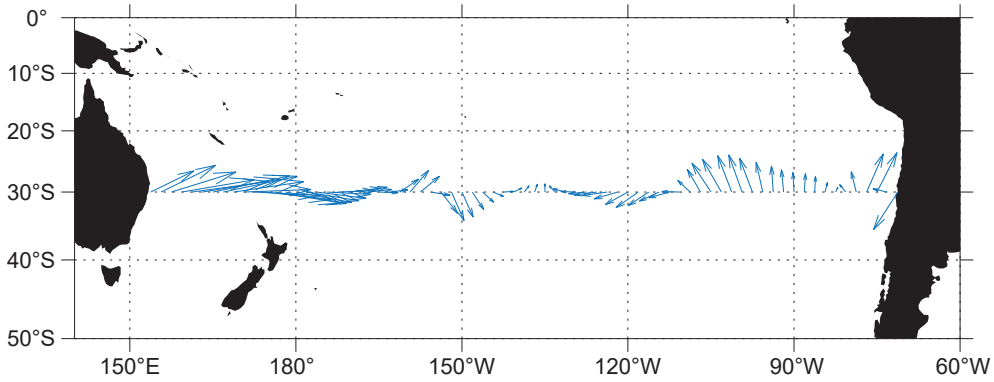

Figure 2. Surface winds at 30ºS in the Pacific Ocean during the cruise period.

Transpacific vertical sections of potential temperature, salinity, neutral density, oxygen and silicate (Figures 3-7) and θ-S diagrams of all stations and of four selected stations (Figure 8) are used to identify the existing water masses in the South Pacific Ocean following Talley et al. (2011).

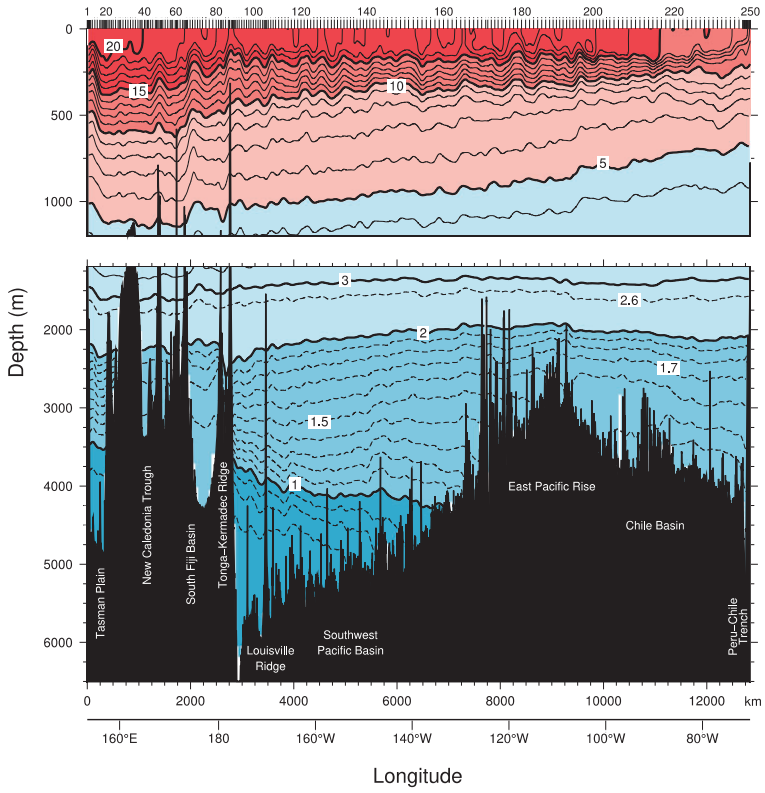

Figure 3. Vertical section of θ (ºC) at 32ºS in the Pacific Ocean for data collected in 2017. Tick-marks on the top axis indicate the location of stations.

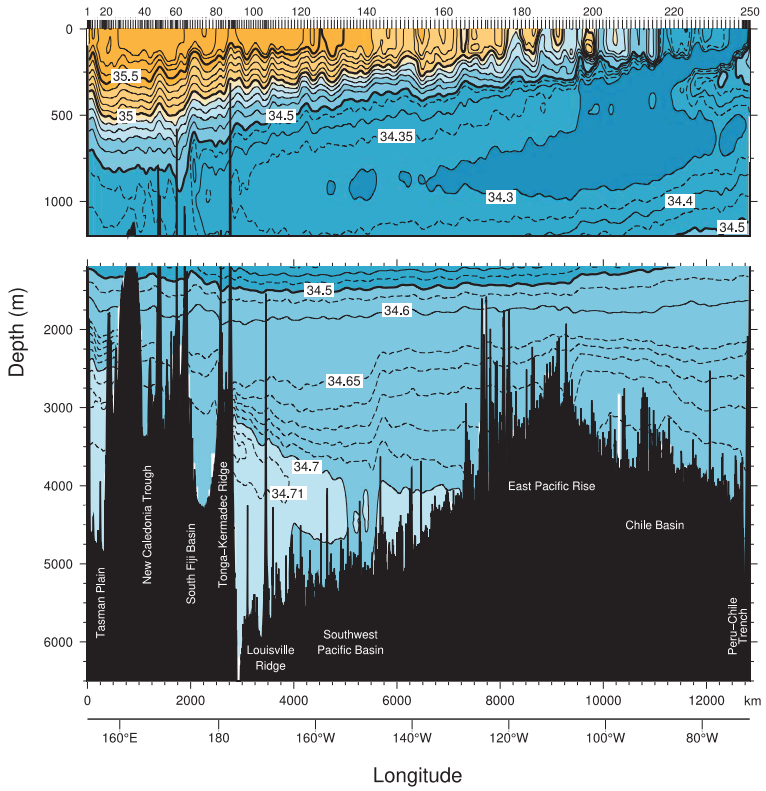

Figure 4. Vertical section of salinity at 32ºS in the Pacific Ocean for data collected in 2017. Tick-marks on the top axis indicate the location of stations.

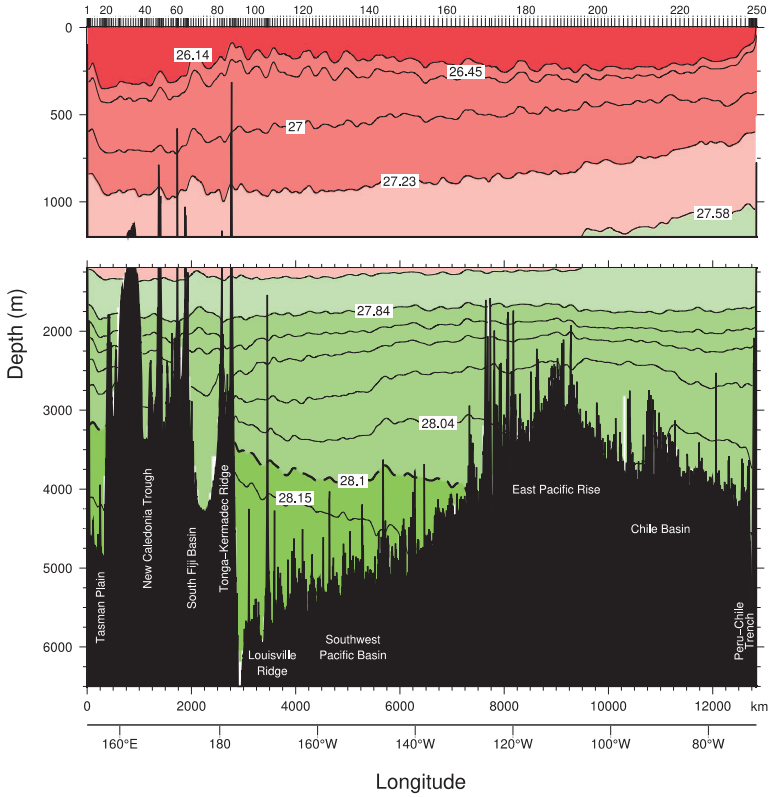

Figure 5. Vertical section of neutral density (γ^n) at 32ºS in the Pacific Ocean for data collected in 2017. Tick-marks on the top axis indicate the location of stations. The isopycnals labeled are the γ^n layers used to estimate the geostrophic transport.

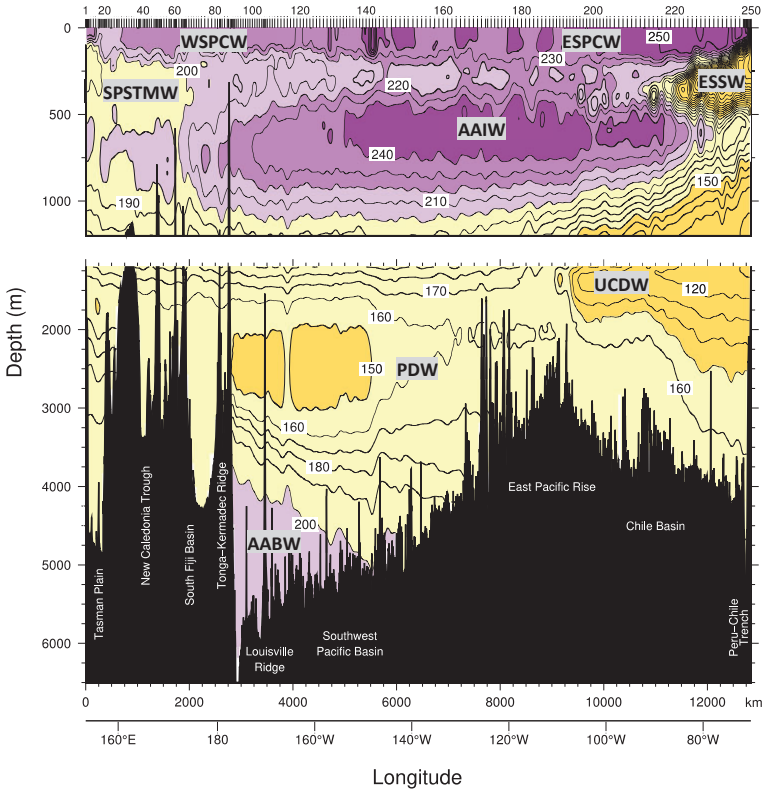

Figure 6. Vertical section of oxygen (µmol/kg) at 32ºS in the Pacific Ocean for data collected in 2017. Tick-marks on the top axis indicate the location of stations. The water masses identified are: South Pacific Subtropical Mode Water (SPSTMW), Equatorial Subsurface Water (ESSW), Eastern South Pacific Central Water (ESPCW), Western South Pacific Central Water (WSPCW), Antarctic Intermediate Water (AAIW), Upper Circumpolar Deep Water (UCDW), Pacific Deep Water (PDW), and Antarctic Bottom Water (AABW).

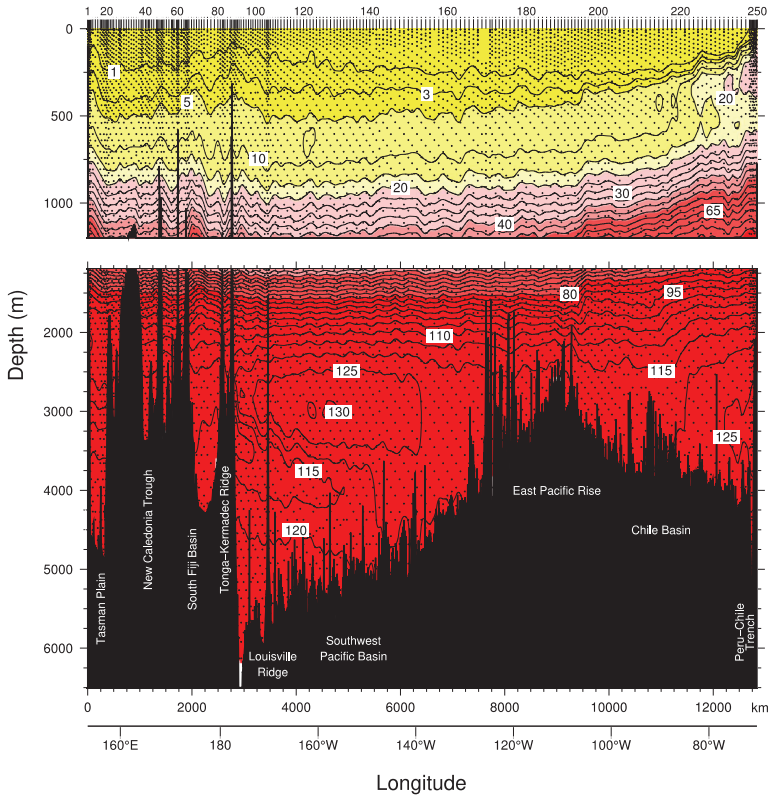

Figure 7. Vertical section of silicate (µmol/kg) at 32ºS in the Pacific Ocean for data collected in 2017. Tick-marks on the top axis indicate the location of stations.

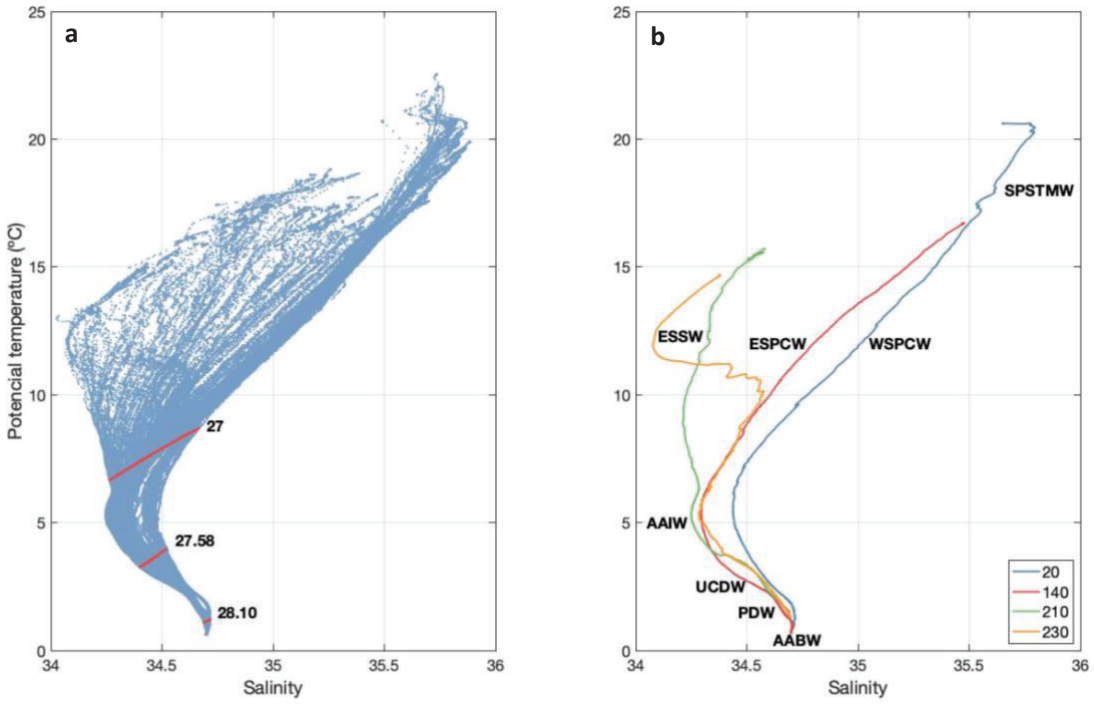

Figure 8. θ-S diagrams using all the stations of the cruise (a) and using only four the stations (b) at 32ºS in the Pacific Ocean for data collected in 2017. The water masses identified are: South Pacific Subtropical Mode Water (SPSTMW), Equatorial Subsurface Water (ESSW), Eastern South Pacific Central Water (ESPCW), Western South Pacific Central Water (WSPCW), Antarctic Intermediate Water (AAIW), Upper Circumpolar Deep Water (UCDW), Pacific Deep Water (PDW), and Antarctic Bottom Water (AABW).

In the upper layer, between the surface and γ^n=27.00 kg/m^3 (above ~500 m depth, figure 5) the South Pacific Central Water (SPCW) is found with high salinity values (Figure 4 and 8), which is characterized with subtropical thermocline waters formed by subduction (Talley et al., 2011). The SPCW can be divided into two different water masses: Western South Pacific Central Water (WSPCW) and Eastern South Pacific Central Water (ESPCW). The WSPCW (S>35) is separated from the eastern boundary by the fresher ESPCW (35<S<34.3), advected northward from fresher high latitude surface waters (Emery, 2001; Emery & Meincke, 1986; Sprintall & Tomczak, 1993).

Furthermore, the South Pacific Subtropical Mode Water (SPSTMW) is found between the surface and γ^n=26.45 kg/m^3 (Figure 5), that corresponds to ~0-300 m depth. SPSTMW is formed by the subduction of thick winter mixed layer and characterized in the vertical by low levels of oxygen (<200 µmol/kg, figure 6) and temperatures of about 15ºC-19ºC (Figure 3 and 8). This water mass -found in the west side of the vertical sections- is present north of the Tasman Front and East Auckland Current (Roemmich & Cornuelle, 1992; Talley et al., 2011). The Tasman Front extends across the Tasman Sea to the northernmost point of New Zealand and forms the East

Auckland Current that flows the northeast coastline of New Zealand's North Island (Heath, 1985; Tilburg et al., 2001).

The Equatorial Subsurface Water (ESSW), found in coastal regions between 26.45 kg/m^3< γ^n <27.00 kg/m^3 from about 300 to 370 m depth (Figure 5), is formed near the equator by vertical mixing of waters. The ESSW is carried eastward by the Equatorial Undercurrent and the Southern Subsurface Countercurrent, and then the Peru-Chile Undercurrents and Peru-Chile Countercurrents transport ESSW southward to approximately 48°S (Montes et al., 2010; Neshyba, 1979; Stramma et al., 2010; Tsuchiya & Talley, 1998; Wyrtki, 1967). ESSW is characterized with temperatures of about 8.5°C-10.5°C (Figure 3 and 8), relatively low salinities (34.4-34.8, figure 4) and extremely low oxygen values (<150 μmol/kg, figure 6) (Brink & Robinson, 2005; Silva et al., 2009).

Below this layer, in the intermediate waters (between 27.00 kg/m^3< γ^n <27.58 kg/m^3, figure 5), that corresponds to ~500-1000 m depth, the Antarctic Intermediate Water (AAIW) is located, which is formed by advection of fresh Subantarctic Surface Waters (SASW). The AAIW is a relatively cold water mass with temperatures of about 5-10°C (Figure 3 and 8), and it is characterized in the vertical by the minimum salinity values (<34.5, figure 4), high oxygen concentration (>220 μmol/kg, figure 6), and low silicate concentration (<20 μmol/kg, figure 7) (Talley et al., 2011; Tsuchiya, 1990; Tsuchiya & Talley, 1996).

In the deep layer, with a neutral density range of 27.58 kg/m^3< γ^n<28.10 kg/m^3 (Figure 5), extending from about 1000-4000 m depth, is found the Pacific Deep Water (PDW), which is formed by mixing and aging of deep waters that flow into the Southern Ocean. Because of PDW formation, the waters in the PDW are the oldest of the global ocean. The PDW is characterized in the vertical by low levels of oxygen (~150 μmol/kg, figure 6), salinity values of about 34.5-34.7 (Figure 4 and 8), and the maximum silicate concentration (~125 μmol/kg, figure 7) (Knauss, 1962; Talley et al., 2011; Wijffels et al., 2001).

Specially in the South Pacific, PDW and Upper Circumpolar Deep Water (UCDW) are horizontally juxtaposed. According to Talley et al. (2011), the UCDW is located between 27.58 kg/m^3< γ^n<28.10 kg/m^3 (Figure 5), and extends from about 1000 to 3000 m depth. The UCDW is formed by the mixture of deep waters into the Southern Ocean and is characterized in the vertical by low levels of oxygen (~150 μmol/kg, figure 6), silicate concentration of about 40-115 μmol/kg (Figure 7), and salinity values of ~34.4-34.65 (Figure 4 and 8) (Callahan, 1972; Talley et al., 2011).

The densest water mass in the Pacific, γ^n>28.1 kg/m^3 from approximately 3000 m depth to the seafloor (Figure 5), is called the Lower Circumpolar Deep Water (LCDW), which can also be called as Antarctic Bottom Water (AABW) for global discussion. As stated in Talley et al. (2011), this water mass comes from the Southern Ocean formed by a mixture of the deep waters of all three Oceans: North Atlantic Deep Water (NADW), PDW and Indian Deep Water (IDW). AABW is identified in the Pacific Ocean by low temperatures (<1^{o}C, figure 3 and 8) and high salinity (>34.7, figure 4). Moreover, if compared with PDW, the higher oxygen concentration (200 μmol/kg, figure 6) and lower silicate concentration (~115 μmol/kg, figure 7) of the AABW, indicate that it is significantly younger than the PDW (Kawano et al., 2006; Talley et al., 2011).

Furthermore, the rising isotherms and isoneutrals in the transatlantic vertical sections allow us to identify the effect of the East Australian Current (EAC) in the western basin, and the Peru-Chile Current in the eastern basin (Figures 3-5).

The East Australian Current (EAC) is an intense western boundary current, with strong velocity shear in the upper 1000 m, flowing southward along the east Australian continental boundary. The common EAC core width has been reported to be approximately 30 km, and recent studies, at approximately 32^{o}S, indicate that most of the EAC poleward transport is confined between the coast and ~155^{o}E, with a northward return flow to the east of the boundary current (Chiswell et al., 1997; Hernández-Guerra & Talley, 2016; Ridgway & Godfrey, 1994; Talley et al., 2011). Moreover, the EAC is associated with most of the very strong eddies and instabilities found in the P06 section, and occasionally it is difficult to define the continuous path for the current (Mulhearn, 1987; Wijffels et al., 2001).

The Peru-Chile Current is a narrow eastern boundary current. It is evident in the upward slope of the isotherms and isoneutrals surfaces in the upper water (>700 m) off the west coast of South America (Strub et al., 1998; Tsimplis et al., 1998). Below this current, approximately between 200-1000 m depth (Wooster & Reid, 1963), is found the Peru-Chile Undercurrent, a subsurface poleward flow associated with the ESSW (Wooster & Gilmartin, 1961) marked in the downward slope of the isotherms and isoneutrals (Shaffer et al., 1999).

3. RELATIVE GEOSTROPHIC TRANSPORT AND INVERSE MODEL

The thermal wind equation is used to compute the relative geostrophic velocity profile at each station pair, with a reference layer of no motion chosen at the neutral

density γ^n=28.1 kg/m^3 (dashed contour in figure 5). This layer, also known as ZVS "Zero Velociy Surface", is the same used in previous studies carried out using hydrographic data at 30ºS in the Atlantic, Pacific and Indian Oceans (Ganachaud, 2003; Hernández-Guerra & Talley, 2016; Hernández-Guerra et al., 2019). If the deepest common level of the stations pairs is shallower than the reference layer, the bottom is used as the initial reference level of no motion. Below the deepest common depth of each station pair, velocities are considered to be constant. In addition, to estimate the velocity at the reference layer and to constrain the mass transport in the boundary currents, SADCP and LADCP data are used (Comas-Rodríguez et al., 2010; Joyce et al., 2001; Wijffels et al., 1998).

Figure 8 shows a comparison between the initial geostrophic velocity (dashed black lines), the SADCP velocity between stations (red line), LADCP velocity (blue line) calculated as the mean of the LADCP velocities in each hydrographic station, and the geostrophic velocity adjusted to the SADCP or LADCP velocity (black solid line), with four different adjustment examples. Either if both LADCP and SADCP data agreed (Figure 8a), or just SADCP data do (Figure 8b) with the pattern of the geostrophic velocity, the initial geostrophic velocity is adjusted with SADCP data. While if only LADCP data agree with the pattern of the geostrophic velocity, the initial geostrophic velocity is adjusted with LADCP data (Figure 8c). Nonetheless, if none LADCP and SADCP data agree, the initial geostrophic velocity is not adjusted (Figure 8d).

Following Hernández-Guerra & Talley (2016), Hernández-Guerra et al. (2019) and Talley (2008), mass and property transports are computed for the different isoneutral layers that divide the water column (Figure 5). Ekman transport, which is introduced into the first layer, is computed from the NCEP wind stress (Kalnay et al., 1996) corresponding to the time of the cruise following Hernández-Guerra & Talley (2016).

The initial zonally-integrated mass and silicate transports per layer through 32ºS in the Pacific Ocean are shown in figure 9. The total mass transport presents a northward initial imbalance of 26.3 Sv (Table 2) and presents a northward transport for the upper and bottom layers, and a southward transport at deep layers. The initial silicate transport structure is similar to the mass transport and presents a northward initial imbalance of 801.4 kmol/s (Table 2).

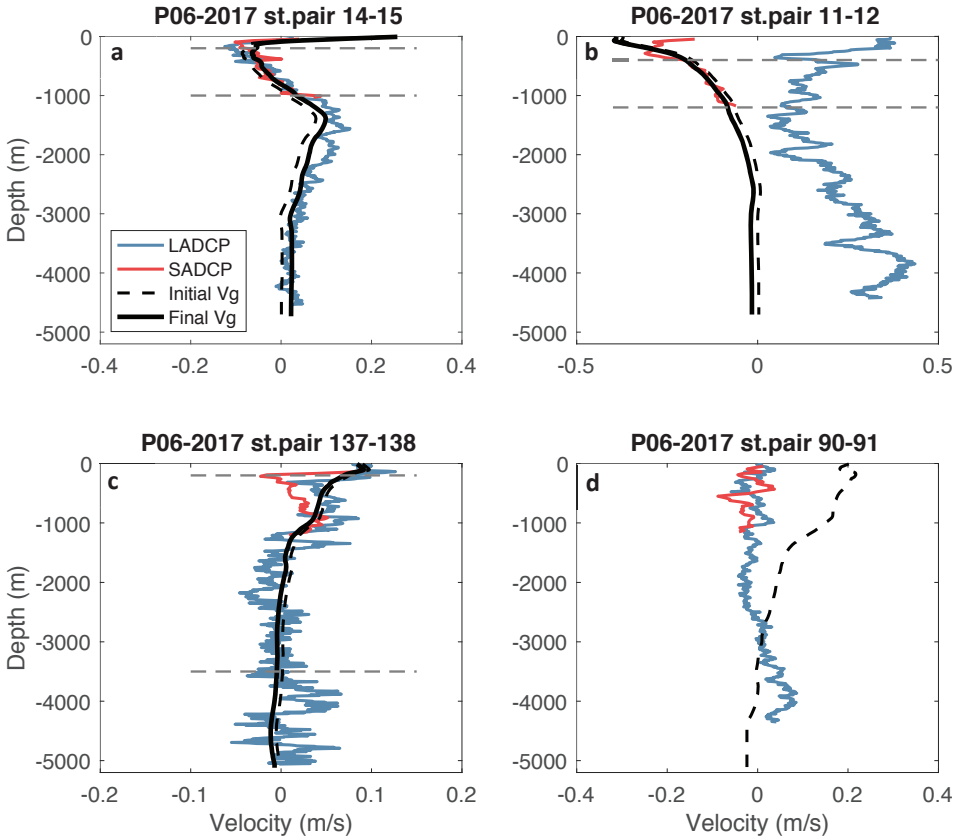

Figure 8. Comparison between the initial geostrophic velocity profile (dashed black lines), the LADCP (blue line) and SADCP (red line) velocity normal to the station pairs, and the geostrophic velocity adjusted with LADCP or SADCP data (black solid line). The subplots correspond to different adjustment examples: (a) both, SADCP and LADCP, data agree, (b) only SADCP data agree, (c) only LADCP data agree, and (d) none agree.

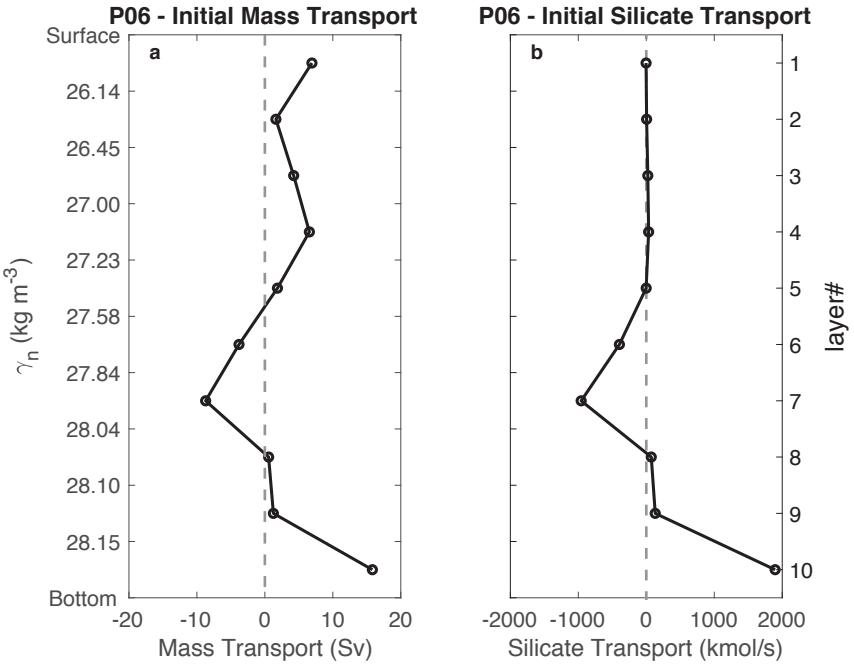

Figure 9. Initial zonally-integrated meridional mass (Sv) (a) and silicate transport (kmol/s) (b) per layer across 32ºS in the Pacific Ocean for data collected in 2017.

In order to reduce this large imbalance, we apply an inverse model to estimate a velocity at the reference layer, subject to chosen constraints and uncertainties (Wunsch, 1978, 1996). The subsequent equation has to be solved:

$$\iint \rho b dx dz = -\iint \rho V_r dx dz + E_k$$

where ρ is the density, b is the unknown reference velocity, V_r is the relative geostrophic velocity obtained from the thermal wind equation, E_k is the Ekman transport normal to the section, and x and z designate the along-section and vertical coordinates, respectively.

This procedure provides one single equation for each vertically integrated mass and silica conservation with 248 unknowns (the number of station pairs). In addition to total mass and silica conservation, we introduced several regional constraints for different longitude and depth ranges, listed in table 2. Previous studies of earlier occupations of these sections in the Pacific (Hernández-Guerra & Talley, 2016; Wijffels et al., 2001) included assorted mass transport constraints in specific longitude ranges and depths from independent data. These come from independent estimates of ITF (Gordon et al., 2010; Sprintall et al., 2009), large northward transport for the narrow Deep Western Boundary Current (DWBC) just east of the Tonga-Kermadec Ridge (TKR) (Whitworth et al., 1999), and silica transport constraint (Talley & Sprintall, 2005).

The solution of the inverse model follows the first approach developed in Joyce et al. (2001) and subsequently carried out by Hernández-Guerra & Talley (2016) and Hernández-Guerra et al. (2019) with some specific differences. The closed box for the inverse model is formed by the transpacific 32ºS section plus the ITF and Bering Strait transport. The full matrix equation and its derivation is provided in the Appendix A. Following Wunsch (1996), the inverse problem is solved through the Gauss-Markov method, which asks *a priori* variance for each equation and solution. The *a priori* velocity variance for the solution is (2 cm/s)^2 throughout, exept in regions with strong shear that is (4 cm/s)^2, corresponding to the EAC and the DWBC. The *a priori* variance of each equation is shown in table 2.

The velocity at the reference level estimated from SADCP and LADCP data and from the inverse model are presented in figure 10. The adjusted velocities from ADCP data (Figure 10a) are higher than the velocities from the inverse model (Figure 10b), which are not significantly different from zero at all stations as in previous inverse

models (Hernández-Guerra & Talley, 2016; Hernández-Guerra et al., 2019). Thus, ADCP data adjustment has definitely more relevance.

Table 2. Regional transport constraints and inverse model results for the Pacific Ocean (P06) at 32ºS in 2017. Positive transports are northward and negative transports are southward. Initial transports relative to the ZVS at γ^n=28.1 kg/m^3 and final transports are listed.

P06 - 2017	Property	Longitude	Layers	Constraint	Initial	Final
Total mass[1]	ITF and Bering Strait transport (Sv)	All	1:10	15 ± 5	26.3	15.3 ± 10.4
Silicate conservation[2]	Total Silicate (kmol/s)	All	1:10	120 ± 20	801.4	0.1 ± 256
Deep transport[3]	Tasman Sea (Sv)	150-161ºE	9:10	0.5 ± 0.5	0.1	1.2 ± 0.5
Deep transport[3]	Tasman Sea (Sv)	161-173ºE	7:10	0 ± 0.5	1.2	0.0 ± 0.5
Deep transport[3]	Tasman Sea (Sv)	173-181ºE	7:10	0 ± 0.5	1.5	0.0 ± 0.5
Deep transport[3]	Eastern Basin (Sv)	110-70ºW	8:10	0.75 ± 0.75	-0.8	0.7 ± 0.7
DWBC constraint[4]	Tonga-Kermadec Ridge (Sv)	180-168ºW	8:10	15 ± 4	13.5	13.5 ± 3.1

[1]ITF transport from Gordon et al. (2010) and Sprintall et al. (2009).
[2]Silicate conservation from Talley & Sprintall (2005).
[3]Deep transport constraints from Wijffels et al. (2001).
[4]DWBC constraint from Whitworth et al. (1999).

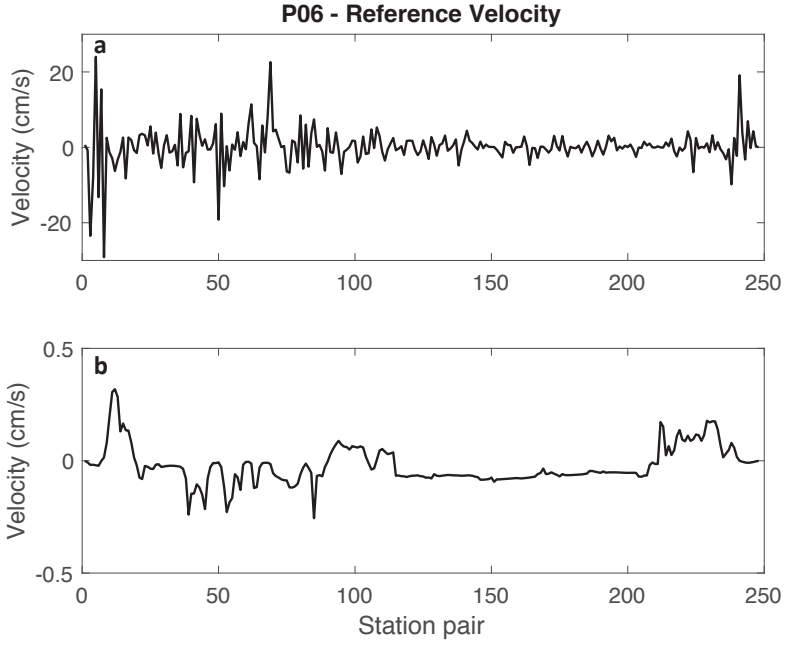

Figure 10. Geostrophic velocity (cm/s) adjusted to the SADCP or LADCP data (a) and reference velocities from the inverse model (b) at each station pair for 2017 P06 section at nominally 32ºS in the Pacific Ocean.

4. FINAL ADJUSTED TRANSPORT

4.1 Meridional transport per layer

Figure 11 shows the final mass and silicate transports per neutral density layer from the inverse model. The net initial mass and silicate transports imbalances using a reference level of γ^n=28.1 kg/m^3 (26.3 Sv and 801.4 kmol/s, respectively) are greatly reduced (15.3 ± 10.4 Sv and 0.1 ± 256 kmol/s, respectively) as seen from the total transports in table 2. Thus, the final transports satisfy the constraints within the applied uncertainty. Results show the same pattern as previous analyses of the meridional overturning circulation at this latitude for 2003 and 2009 (Hernández-Guerra & Talley, 2016): northward mass transport in the upper (Layers 1-5) and abyssal layers (Layers 9-10), and southward mass transport in the deep layers (Layers 6-8). In 2017, the layer 8 has a slight northward transport due to the warming in abyssal layers (Purkey et al., 2019), but it has been included in the deep layers according to its density following Hernández-Guerra & Talley (2016). It is worth nothing that 2003 and 2017 show a roughly similar transport and different to 2009.

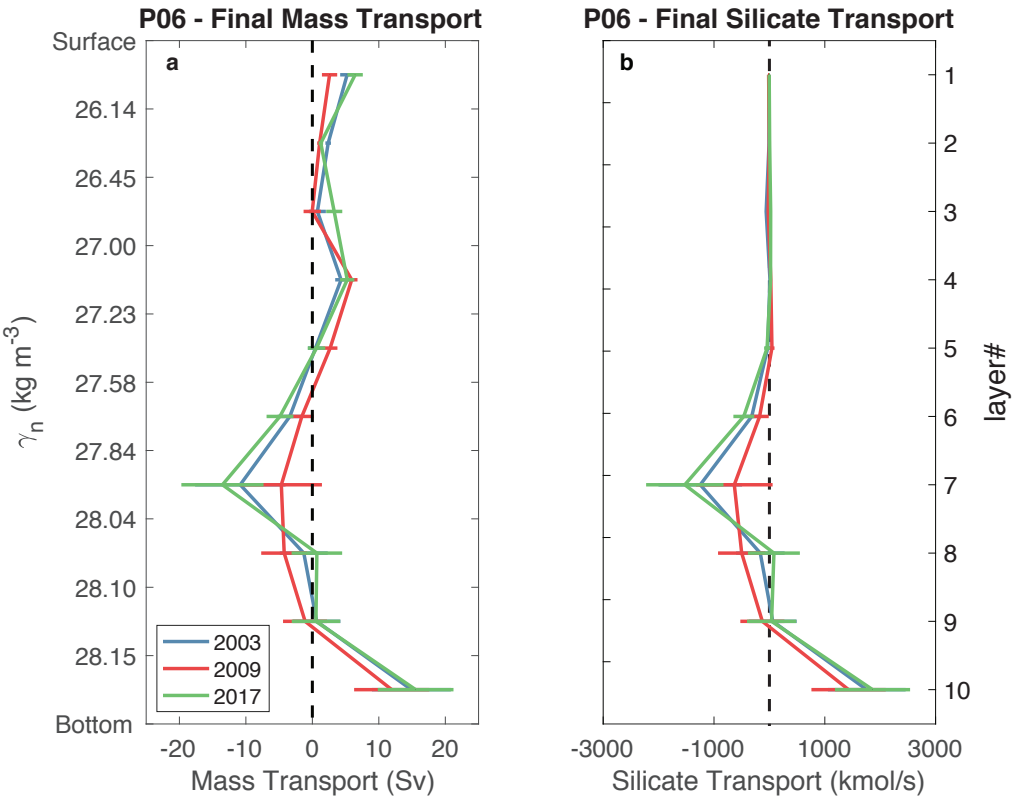

Figure 11. Final zonal-integrated meridional mass transport (Sv) (a) and silicate transport (kmol/s) (b) per layer, with error bars, across 32ºS in the Pacific Ocean for data collected in 2003, 2009 and 2017.

Inverse model results show that deep northward flow in the Pacific section is bottom intensified (Figure 11), with a northward flow of 16.8 ± 7.8 Sv for 2017. This deep Pacific transport is consistent with previous estimates. At 32ºS from WOCE sections, Tsimplis et al. (1998) and Wijffels et al. (2001) estimated a net northward inflow of about 12 and 18 ± 2 Sv, respectively. Using the 1968 Scorpio sections Wunsch et al. (1983) estimated an inflow of 12 Sv in the lower layers. Using Reid (1997)'s absolute geostrophic velocity for the Scorpio sections, Talley et al. (2003) estimated a deep inflow of 10 Sv. However, a more moderate inflow of 7 ± 2 Sv at 32ºS in 1992 was estimated with a global inverse model by Ganachaud & Wunsch (2000). More recently, with a global inverse model, Lumpkin & Speer (2007) presents a stronger inflow of 14.9 ± 3.4 Sv. Also, using an inverse model in the Pacific for the 2003 circumpolar section, Katsumata & Fukasawa (2011) obtained a Pacific deep inflow of 10 Sv below γ^n=28.0 kg/m^3, which was larger than their 8 Sv result for the 1993 WOCE occupation. Most recently, Hernández-Guerra & Talley (2016) estimated a net northward deep inflow of 15.5 ± 6.9 Sv for 2003, 10.8 ± 6.5 Sv for 2009 from hydrographic data in the P06 section.

The adjusted silicate transport (Figure 11b) follows the same structure of mass transport (Figure 11a). There is a northward silicate transport in the deepest layers (Layers 8-10) and a southward transport in the mid-depth layers (Layers 6-7) that extends up into the upper layers (Layer 5). Low silicate transports in the uppermost layers (Layers 1–4) result from very low silicate values in the first 1000 m of the water column. Again, silicate transport results show the same pattern as 2003 and 2009 results computed by Hernández-Guerra & Talley (2016), with a roughly similar transport in years 2003 and 2017.

4.2 Meridional Overturning transport

The meridional overturning transport across 32ºS for the Pacific Ocean is computed by vertically integrating the mass transport from the bottom to the surface of the ocean (Figure 12). The intensity of the overturning is generally described as the maximum in the overturning stream function (zonally averaged transport integrated from the surface down), comprising northward flowing within the South Pacific Ocean and returning southward flow as PDW (~1500-3000 m). The resulting overturning stream function for 2003 and 2009, computed by Hernández-Guerra & Talley (2016), present a nearly zero net flow in layer 3, which is probably a balance between net northward flow for the ITF and net southward flow in the thermocline associated with the shallow overturn of the subtropical gyre (Talley, 2008, 2003), that cannot be

observed in our results for 2017. The overturning circulation in 2017 shows the same pattern as in 2003 and in 2009, but the intensity of the overturning in 2009 (43.6 ± 2.3 Sv) is higher than in 2003 (32.1 ± 2.2 Sv) and in 2017 (34.9 ± 2.4 Sv), showing these two years a non-significant overturning difference.

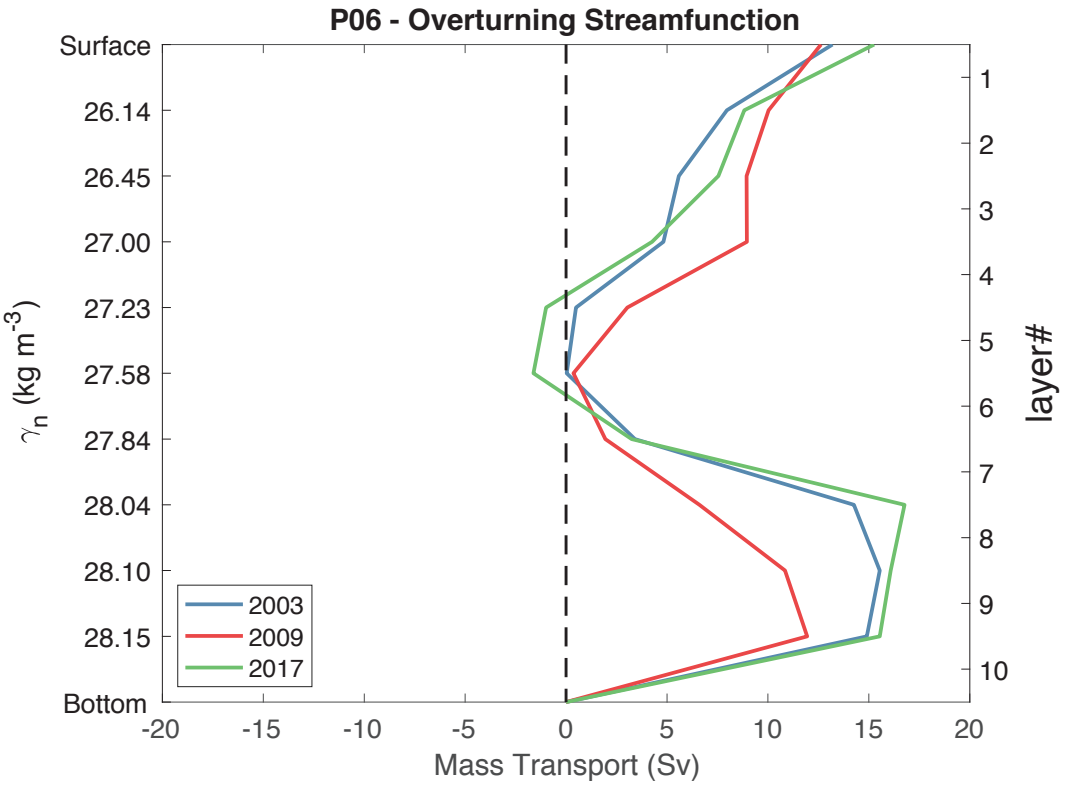

Figure 12. Overturning mass transports stream function across 32ºS in the Pacific Ocean for 2003, 2009 and 2017. This function is computed as the zonally- and vertically-integrated mass transports in isoneutral layers (along the entire section and from the seafloor to the sea surface).

5. HORIZONTAL DISTRIBUTION OF FINAL ADJUSTED TRANSPORT

Figure 13 shows the horizontal distribution of meridional transport in isopycnal layers for 2017 and for 2003 and 2009 computed by Hernández-Guerra & Talley (2016). This distribution is obtained by integrating the mass transport in each layer eastward from zero at the western boundary, and then summing transports in layers that have overall transport to the north and to the south. Thus, the Pacific Ocean is divided into three-layer sets (Figure 13): northward transport in the uppermost layers (1-5), southward in the deep layers (6-8), and northward in the bottom layers (9-10).

5.1 Upper ocean circulation

The accumulated upper ocean mass transport (Figure 13a), consisting of thermocline and intermediate waters (surface to γ^n=27.58 kg/m^3, about 1140 m depth), shows the usual subtropical gyre feature: an intense western boundary current flowing poleward, an equatorward recirculation east and close to the western boundary, and a net equatorward transport across the ocean interior with a wide and slow Peru-Chile Current in the eastern boundary. Alternating transports due to eddies are not very strong, but are intensified in the westernmost part of the circulation, corresponding to the Tasman Sea (as noted in both Hernández-Guerra & Talley (2016) and Wijffels et al. (2001)).

5.1.1 Interior gyre circulation

The Pacific Ocean interior circulation (Figure 13a) for 2003 and 2017 differ noticeably from 2009. These marked differences are also found in deep and bottom layers mass transports (Figure 13b and c). West of the TKR, located at approximately 178°W encompassing the Tasman Sea and South Fiji Basin, the horizontal mass transports for the three years are similar, with net southward transport dominated by the southward EAC and a major eddy field. The circulation from the surface to the bottom of the ocean of 2009 significantly diverges across the mid-Pacific, between the TKR and the East Pacific Rise (EPR) at 110°W, from 2003 and 2017. In the upper layers, the 2003 transport is a "classic gyre" with a northward transport from the TKR to the EPR, whereas in 2009 the structure of the mass transport is a "bowed gyre", reaching maximum southward at 155°W, then rebounding with compensating northward transport (Hernández-Guerra & Talley, 2016). The pattern of the circulation in 2017 has changed from the "bowed" circulation found in 2009, and ressembles that "classic gyre" of 2003. The transports for the three years seem to coalesce at the EPR, reaching northward transports in the eastern boundary of 13.2 ± 2.2 Sv in 2003, 12.3 ± 2.3 Sv in 2009 and 16.9 ± 2.4 Sv in 2017. Thus, the net norward transport obtained in 2017 is comparable with the estimated transport of both 2003 and 2009. The "bowed gyre", subject to significant interannual variability (McCarthy et al., 2000), was previously observed by Wyrtki (1975) with a classic surface dynamic, and by McCarthy et al. (2000) and Wijffels et al. (2001) in the original WOCE P06 section in 1992. While Reid (1997)'s surface circulation instead of showing the "bowed gyre", showed a circulation similar to both 2003 and 2017.

5.1.2 Western boundary current: East Australian Current

The East Australian Current (EAC) recirculation results in a relative intense net southward transport near the western boundary in the South Pacific Ocean. According to Hernández-Guerra & Talley (2016), the EAC is summed over both upper and deep layers (Layers 1-8) and has a net transport of -39.2 ± 1.6 Sv in 2017 (Table 4, figure 13a). The maximum of southward mass transport is found at 156.6ºE in 2017 in a roughly similar location found in 2003 by Hernández-Guerra & Talley (2016), showing a shift from the maximum position in 2009 as also reported by Chiswell et al. (1997). Moreover, our EAC transport for 2017 is comparable to previous estimates for the 1992 WOCE P06 section as the -40 ± 8 Sv reported by Macdonald et al. (2009) using an inverse model of all of the Pacific Ocean WOCE data, and the -36 ± 10 Sv reported by Ganachaud & Wunsch (2003) using a global inverse model with WOCE data. However, Wijffels et al. (2001) reported a much weaker EAC transport for the early 1990s of 22.1 ± 4.6 Sv, with an rms variability of 32 Sv estimated from altimetry, based on their 1991–1994 current meter study accompanied by ten EAC hydrographic sections from the coast of Australia to 154.4ºE (Mata et al., 2000). Most recently, Hernández-Guerra & Talley (2016) estimated a stronger EAC transport of -51.1 ± 2.0 Sv and -49.9 ± 2.1 Sv using an inverse model with GO-SHIP data for 2003 and 2009, respectively (listed in table 4).

5.1.3 Eastern boundary current: Peru-Chile Current and Peru-Chile Undercurrent

As the variability induced by the eddy field in any eastern boundary current is strong, similar but more intense than the Canary Current in the North Atlantic Subtropical Gyre (Hernández-Guerra et al., 2017, 2005; Vélez-Belchí et al., 2017), the eastern boundary current in the Pacific Ocean is difficult to discern in the transport figures. The equatorward Peru-Chile Current is evident in the upward slope of the surface isotherms and isoneutral surfaces off the west coast of South America (Figures 3 and 5) (Strub et al., 1998; Talley et al., 2011). The Peru-Chile Undercurrent is found below it and extends over the continental shelf and slope, where the isotherms and isoneutral surfaces slope downward (Shaffer et al., 1999). Following Hernández-Guerra & Talley (2016), the Peru-Chile Current is estimated from the surface to γ^n=27.0 kg/m^3 (Layers 1-3) and from 85ºW to the coast of Chile, and the Peru-Chile Undercurrent from layers 4-5 and from 75ºW to Chile (Table 4). Additionally, the flow of Peru-Chile Current is estimated to be 4.4 ± 0.8 Sv in 2017, which is slightly higher but not significantly different from the result of 2003 (3.3 ± 0.9 Sv) and significantly different from 2009 (2.3 ± 0.8 Sv) estimated by Hernández-Guerra & Talley (2016). Otherwise, the Peru-Chile Undercurrent is estimated

to have a mass transport of about -1.5 ± 0.8 Sv, which is lower but not significantly different from the transport of 2003 (2.8 ± 1.2 Sv) and significantly different from 2009 (3.8 ± 1.2 Sv) (Hernández-Guerra & Talley, 2016).

5.2 Deep ocean circulation

Figure 13b shows the accumulated mass transport for the PDW layers, considered as those depths layers that flow south (Layers 6-8). The net southward mass transport of PDW through 32°S in 2017 (-17.7 ± 7.5 Sv) is slightly higher but not significantly different than in years 2003 (-15.5 ± 7.9 Sv) and 2009 (-10.5 ± 7.3 Sv). The overall horizontal structure for the 2017 was remarkably different from 2009, but similar to 2003. In 2003 and in 2017, the ‘‘straight” gyre years, net southward transport was mostly accomplished by gradual accumulation across the width of the section. While in 2009, the ‘‘bowed” gyre year, the large southward transport in the Southwest Pacific Basin (of about 25 to 40 Sv) was compensated by northward flow across most of the Pacific to about 78°W, and next a southward flow in the Peru–Chile Current system, restoring the net transport to its overall level (Hernández-Guerra & Talley, 2016).

5.3 Abyssal ocean circulation

Figure 13c presents the accumulated mass transport for the AABW layers. The mass transport for layers 9 and 10 shows a northward flow into the Pacific between the TKR and the EPR (Figure 11a), and therefore, these layers are considered as the bottom layers (γ^n>28.1 kg/m^3). The net abyssal northward transport in 2017 is 16.1 ± 6.8 Sv, which is not significantly different from those of 2003 (15.5 ± 6.9 Sv) and 2009 (10.8 ± 6.5 Sv) estimated by Hernández-Guerra & Talley (2016). In 2017, the northward transport was broadly distributed over the deepest part of the Southwest Pacific Basin as in 2003. However, most of the northward transport in 2009 was in the narrow DWBC, which resembles Reid (1997)’s abyssal circulation maps based on a 1968 hydrographic section (with a strong northward DWBC) and Wijffels et al. (2001) solutions for the 1992 WOCE P06 section.

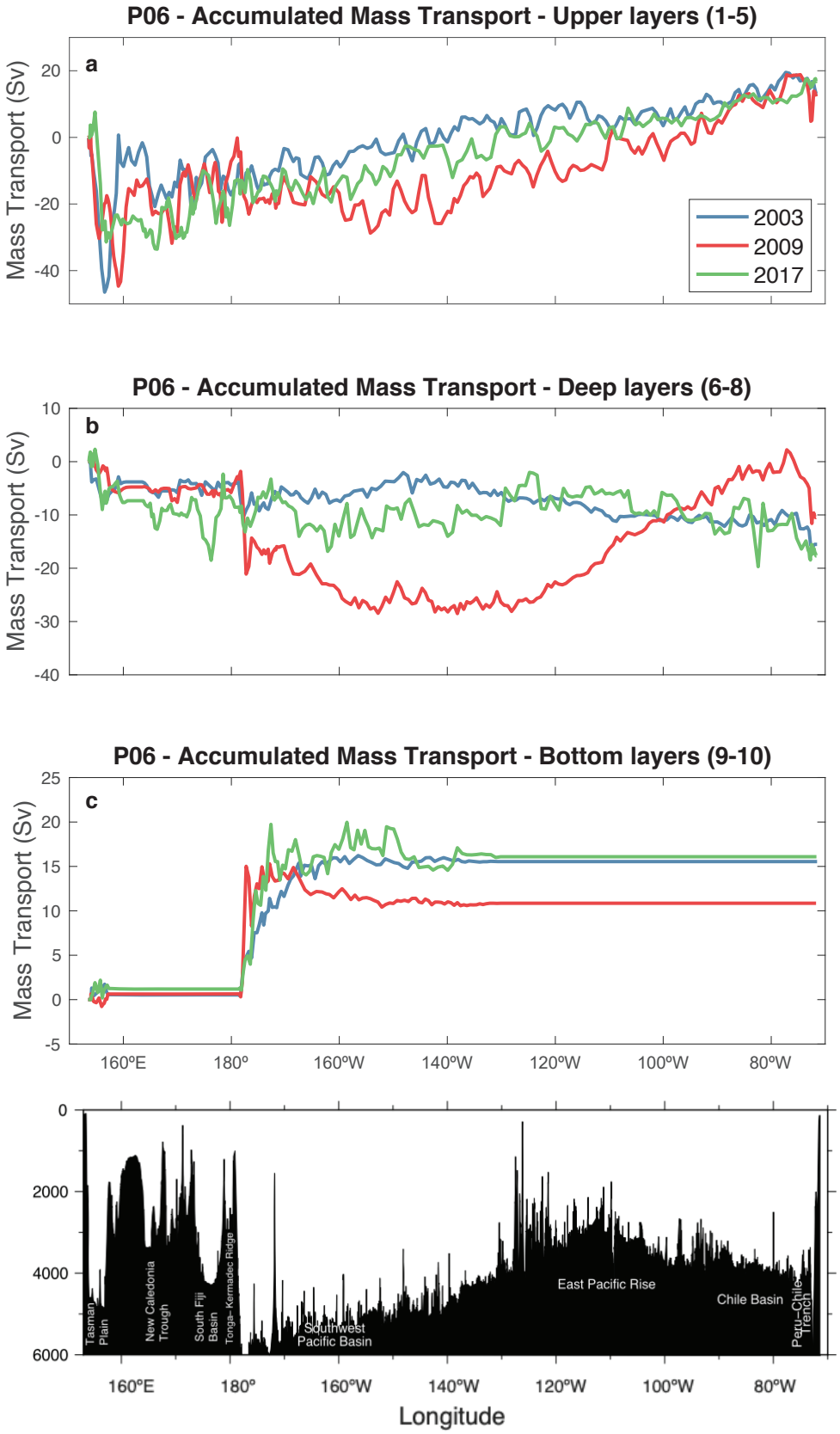

Figure 13. Eastward accumulated mass transport (Sv) at 32°S for (a) upper, (b) deep, and (c) bottom layers for 2003, 2009 and 2017. Bottom plot shows the bathymetry for reference.

Table 4. Mass transports inverse model results and uncertainty (Sv) for the East Australian Current, Peru-Chile Current and Peru-Chile Undercurrent for the Pacific Ocean (P06) at 32°S in 2003, 2009 and 2017. Positive transports are northward and negative transports are southward.

Mass Transport (Sv)	Longitude	Layers	Final 2003[1]	Final 2009[1]	Final 2017
East Autralian Current	Coast to 156.7°E (2003) 158.9°E (2009) 156.6°E (2017)	1:8	-51.1 ± 2.0	-46.1 ± 2.1	-39.2 ± 1.6
Peru-Chile Current	85°W to coast	1:3	3.3 ± 0.9	2.3 ± 0.8	4.4 ± 0.8
Peru-Chile Undercurrent	75°W to coast	4:5	-2.8 ± 1.2	-3.8 ± 1.2	-1.5 ± 0.8

[1]Final mass transports computed by Hernández-Guerra & Talley (2016).

5.4 Origin of the change in zonal structure of the transports

The Hovmöller diagram (Figure 14) presents the AVISO Absolute Dynamic Topography (ADT) Sea Surface Height (SSH) along 30°S from January 1993 to April 2019, which shows a high SSH in the western boundary and low at the eastern boundary, hence yielding equatorward transport in the upper ocean. It is also observed an overall trend toward higher SSH between New Zealand (NZ) and EPR. The high SSH found between 150°E to 170°E is associated with topography just north of NZ, and the Tasman Sea to the west of this is much more eddy-rich than the interior of the South Pacific Ocean. Superimposed on these signals are large-scale, west-propagating disturbances of 10-15 cm amplitude, with time scales of several years as noted in Hernández-Guerra & Talley (2016). These disturbances are initiated in the eastern Pacific, at 90-100°W and propagate westward, taking approximately 7-10 years to cross the 7000 km to NZ, hence a speed of ∼3 cm/s. This is approximately the speed of the long baroclinic Rossby waves at this latitude (Chelton et al., 2011). As indicated in Hernández-Guerra & Talley (2016) for 2003 and 2009, the 2003 P06 section was occupied when an anomalously lower SSH was centred over the EPR and a high SSH over the Southwest Pacific Basin; while the 2009 P06 occurred when the particularly high ridge had arrived at the central Pacific between 160°W and 140°W, with lower SSH to the east and to the west. The 2017 P06 occurred during a period with a similar 2003 distribution of SSH, lower SSH over the EPR and high SSH over the Southwest Pacific Basin.

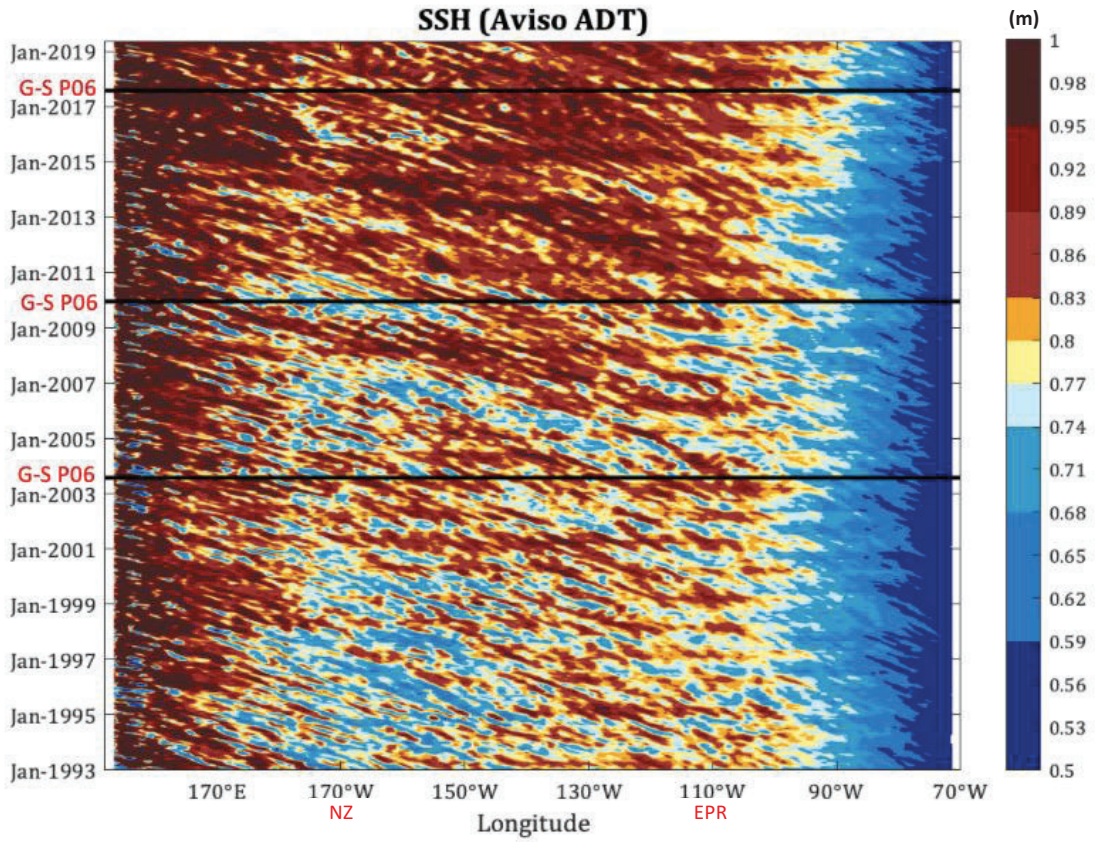

Figure 14. South Pacific absolute dynamic topography (m) along 30ºS for the altimetry complete time series from January 1993 to April 2019. The P06 cruise periods in 2003, 2009, and 2017 are indicated. The longitudes of New Zealand (NZ) and East Pacific Rise (EPR) are also indicated. Merged AVISO product (http://las.aviso.oceanobs.com).

6. HEAT AND FRESHWATER TRANSPORTS

Table 5 shows a comparison of our heat transport (PW) and freshwater flux (Sv) results for the Pacific Ocean (P06) in 2017 with those estimated by Hernández-Guerra & Talley (2016) for 2003 and 2009. Meridional heat transports across the P06 section from our inverse model indicate that the northward heat transport in 2017 (0.4 ± 0.1 PW) has the same value as in 2003 (0.4 ± 0.1 PW) and differs from the heat transport obtained in 2009 (0.2 ± 0.1 PW), both estimated by Hernández-Guerra & Talley (2016).

The freshwater flux is estimated following Joyce et al. (2001):

$$\bar{F} = \sum_i \sum_j T_{ij} S'_{ij} / S_0$$

where T_{ij} is the absolute mass transport, S'_{ij} is the anomaly of salinity (Salinity-S_0), both in layer i at station pair j. S_0 is the global ocean mean salinity (34.9 used by Hernández-

Guerra & Talley (2016) and Talley (2008)). Net freshwater transport (Sv) is equivalent to the net evaporation minus precipitation. Hence the positive freshwater values are caused by higher evaporation than precipitation (freshwater flux from the ocean to the atmosphere). The freshwater results in 2003 (0.25 ± 0.02 Sv) and in 2009 (0.50 ± 0.03 Sv) showed an increase in net evaporation (Hernández-Guerra & Talley, 2016), but our result in 2017 (0.34 ± 0.08 Sv) showed a decrease in net evaporation from 2009.

Table 4. Heat transport (PW) and net freshwater transport (Sv), which is equivalent to the net evaporation minus precipitation (positive is net evaporation), for the Pacific Ocean north of 32°S.

Year	Heat Transport (PW)	Freshwater Flux (Sv)
2003[1]	0.4 ± 0.1	0.25 ± 0.02
2009[1]	0.2 ± 0.1	0.50 ± 0.03
2017	0.4 ± 0.1	0.34 ± 0.08

[1]Heat transports and freshwater fluxes computed by Hernández-Guerra & Talley (2016).

7. DISCUSSION AND CONCLUSION

Four major findings can be highlighted after analysing the changes in meridional transports across 32°S in the Pacific Ocean (P06 section) in 2017 as a result of an inverse model.

First, the zonally-averaged Pacific overturning transport in 2017 shows the same pattern as in 2003 and in 2009, but the intensity of the overturning in 2009 (43.6 ± 2.3 Sv) is higher than in 2003 (32.1 ± 2.2 Sv) and in 2017 (34.9 ± 2.4 Sv), showing these two years a non-significant overturning difference.

The second major finding is that the changes in the shift of the horizontal structure of the Pacific circulation within the different neutral density layers and years (whose shape extended into the bottom layers) are independent of changes in the meridional overturning transport, extending into the deepest layers and including the DWBC, which is part of the overturning circulation. This result suggests that the horizontal and overturning circulations are not coupled and are affected by processes with independent time scales (as noted in Hernández-Guerra & Talley (2016)). The upper ocean shift can be characterized as a transition between a more zonal, regular shape in 2003 to a “bowed” shape in 2009 and again to a regular shape in 2017. Satellite altimetry suggests that these changes are associated with large-scale disturbances of 10-15 cm amplitude that propagate slowly westward at roughly the speed of long baroclinic Rossby waves of 3 cm/s, although the associated shifts in the circulation appear to be

quasi-barotropic, extending to the bottom of the ocean. Additionally, the disturbances seem to be generated in the eastern Pacific, between the East Pacific Rise and South America.

Among other results for the circulation, the East Australian Current has decreased slightly in transport from 2003 (-51.1 ± 2.0 Sv) and 2009 (-49.9 ± 2.1 Sv) to 2017 (-39.2 ± 1.6 Sv), with a very vigorous eddy field across the topographically-complex Tasman Sea between the Australia coast and the Tonga-Kermadec Ridge. Furthermore, the Peru-Chile Current transport in the eastern boundary estimated in 2017 (4.4 ± 0.8 Sv) is slightly higher but not significantly different from the result of 2003 (3.3 ± 0.9 Sv) and significantly different from 2009 (2.3 ± 0.8 Sv) as estimated by Hernández-Guerra & Talley (2016). Similar, the Peru-Chile Undercurrent transport estimated in 2017 (-1.5 ± 0.8 Sv) is lower but not significantly different from the transport of 2003 (2.8 ± 1.2 Sv) and significantly different from 2009 (3.8 ± 1.2 Sv) (Hernández-Guerra & Talley, 2016).

Finally, we also find that the northward heat transport in 2017 (0.4 ± 0.1 PW) has the same value as in 2003 (0.4 ± 0.1 PW) and differs from the heat transport in 2009 (0.2 ± 0.1 PW). For the freshwater transport results, there is an increase in the net evaporation from 2003 (0.25 ± 0.02 Sv) to 2009 (0.50 ± 0.03 Sv) (Hernández-Guerra & Talley, 2016), but our result in 2017 (0.34 ± 0.08 Sv) shows a decrease in net evaporation compared to 2009.

By way of conclusion, the pattern of the circulation in 2017 has changed from the "bowed" circulation found in 2009 and resembles that of 2003, as demonstrated by the comprehensive analysis performed here.

Appendix A

For a given station pair, the absolute geostrophic velocity (v_a), as a function of pressure p, is the sum of a relative velocity (v) and the velocity (b) at the reference level:

$$v_a(p) = v(p) + b$$

At each station pair, the inverse model finds the optimal solution for b. Firstly, the mass conservation is applied for the entire water column:

$$\iint \rho v_a dS = 0$$

$$\iint \rho(v + b) dS = 0 \qquad \text{(A.1a, b, c)}$$

$$\sum_{j=1}^{N}\sum_{q=1}^{Q}\rho_{jq}\left(v_{jq}+b_j\right)a_{jq}=0$$

where the area integral dS is over the entire section area, and the differential version, area is a_{jq} for each station pair j and isopycnal layer q. In (A.1) and consecutive equations, the term $\rho_{jq}v_{jq}$ is first summed over each 2 dbar interval within layer q. For the silicate conservation, these equations are multiplied with the silicate conservation, but additional steps are the same. When total mass is constrained to a particular non-zero value, for instance, the Indonesian Throughflow (ITF) (A.1c) becomes:

$$\sum_{j=1}^{N}\sum_{q=1}^{Q}\rho_{jq}\left(v_{jq}+b_j\right)a_{jq}=M_{Total} \qquad \text{(A. 1d)}$$

where M_{Total} is the total transport constraint, and the limits for layers and station pairs are related to the constraint. The total mass conservation is not exact because of the noise from eddies, internal waves, aliasing, measurements errors, etc.:

$$\sum_{j=1}^{N}\sum_{q=1}^{Q}\rho_{jq}b_j a_{jq}+n_{Total}=-\sum_{j=1}^{N}\sum_{q=1}^{Q}\rho_{jq}v_{jq}a_{jq}+M_{Total} \qquad \text{(A.2)}$$

where n_{Total} is the noise.

The following equations, are obtained considering mass conservation in each layer q:

$$\sum_{j=1}^{N}\rho_{jq}b_j a_{jq}+n_q=-\sum_{j=1}^{N}\rho_{jq}v_{jq}a_{jq}+M_q \qquad q=1,2,\dots,Q \qquad \text{(A.3)}$$

where M_q is the layer transport constraint and n_q is the layer noise. Next, this equation is written as:

$$\sum_{j=1}^{N}e_{jq}b_j+n_q=-y_q \qquad q=1,2,\dots,Q \qquad \text{(A.4)}$$

where:

$$e_{jq}=\rho_{jq}a_{jq}$$

$$y_q=\sum_{j=1}^{N}\rho_{jq}v_{jq}a_{jq}-M_q \qquad \text{(A.5)}$$

For silicate constraints, the e_{jq} elements are multiplied at each point in the layer by silicate concentration. Then the matrix equation is rewritten as:

Ab + n = -Y (A.6)

where **b** is an N x 1 vector of the unknowns (reference velocities), **A** is a (Q + 1) x N matrix, **n** is a (Q + 1) x 1 vector, and **Y** is a (Q + 1) x 1 vector of values calculated from the CTD data and externally imposed mass transports. (Q is for the equations for each layer and the +1 is the equation for conservation of the whole water column.)

After that, the Ekman transport is included in the first layer and the total. Thus, allowing the inverse model to adjust the Ekman transport to the specific conditions of the cruise:

$$\begin{pmatrix} e_{11} & \cdots & e_{1n} & 1 \\ e_{21} & & e_{2n} & 0 \\ \vdots & \ddots & \vdots & \vdots \\ e_{q,1} & & e_{q,n} & 0 \\ e_{q+1,1} & \cdots & e_{q+1,n} & 1 \end{pmatrix} \begin{pmatrix} b_1 \\ \vdots \\ b_n \\ \Delta T_{Ek} \end{pmatrix} = \begin{pmatrix} y_1 + T_{Ek} \\ y_2 \\ \vdots \\ y_q \\ y_{q+1} + T_{Ek} \end{pmatrix}$$

To solve this matrix, the Gauss-Markov estimator is applied (Wunsch, 1996), as in Hernández-Guerra & Talley (2016).

For this inverse model, 7 different constraints are applied, which correspond to mass and silica conservation for the Pacific Ocean, and 5 additional transport constraints (boundary currents and deep flows) (Table 2).

8. REFERENCES

Brink, K. H., & Robinson, A. R. (Eds.). (2005). *The Global Coastal Ocean-Regional Studies and Syntheses* (Vol. 11). Harvard University Press.

Callahan, J. E. (1972). The structure and circulation of deep water in the Antarctic. *Deep Sea Research and Oceanographic Abstracts*, *19*(8), 563–575. https://doi.org/10.1016/0011-7471(72)90040-X.

Chapman, P. (1998). The World Ocean Circulation Experiment (WOCE). *Marine Technology Society Journal*, *32*(3), 23.

Chelton, D. B., Schlax, M. G., & Samelson, R. M. (2011). Global observations of nonlinear mesoscale eddies. *Progress in Oceanography*, *91*(2), 167–216. https://doi.org/10.1016/j.pocean.2011.01.002.

Chiswell, S. M., Toole, J., & Church, J. (1997). Transports across the Tasman Sea from WOCE repeat sections: the East Australian Current 1990-94. *New Zealand Journal of Marine Freshwater Research*, *31*(4), 469–475.

Comas-Rodríguez, I., Hernández-Guerra, A., & McDonagh, E. L. (2010). Referencing geostrophic velocities using ADCP data. *Scientia Marina*, *74*(2), 331–338.

https://doi.org/10.3989/scimar.2010.74n2331.

Emery, W. J. (2001). Water types and water masses. *Encyclopedia of Ocean Sciences*, *6*, 3179–3187.

Emery, W. J., & Meincke, J. (1986). Global water masses-cummary and review. *Oceanologica Acta*, *9*(4), 383–391.

Ganachaud, A. (2003). Large-scale mass transports, water mass formation, and diffusivities estimated from World Ocean Circulation Experiment (WOCE) hydrographic data. *Journal of Geophysical Research*, *108*(C7). https://doi.org/10.1029/2002jc001565.

Ganachaud, A., & Wunsch, C. (2000). Improved estimates of global ocean circulation, heat transport and mixing from hydrographic data. *Nature*, *408*(6811), 453–457.

Ganachaud, A., & Wunsch, C. (2003). Large-Scale Ocean Heat and Freshwater Transports during the World Ocean Circulation Experiment. *Journal of Climate*, *16*, 696–705.

Godfrey, J. S. (1989). A Sverdrup model of the depth-integrated flow for the world ocean allowing for island circulations. *Geophysical & Astrophysical Fluid Dynamics*, *45*(1–2), 89–112.

Gordon, A. L. (1986). Interocean exchange of thermocline water. *Journal of Geophysical Research*, *91 (C4)*, 5037–5046.

Gordon, A. L., Sprintall, J., Van Aken, H. M., Susanto, D., Wijffels, S., Molcard, R., Ffield, W., Pranowo, W., & Wirasantosa, S. (2010). The Indonesian throughflow during 2004–2006 as observed by the INSTANT program. *Dynamics of Atmospheres and Oceans*, *50*(2), 115–128. https://doi.org/10.1016/j.dynatmoce.2009.12.002.

Hamon, B. V., & Tranter, D. J. (1971). East Australian Current. *Australian Natural History*, *17*(4), 129–133. https://doi.org/http://hdl.handle.net/102.100.100/317290?index=1.

Heath, R. A. (1985). A review of the physical oceanography of the seas around New Zealand-1982. *New Zealand Journal of Marine Freshwater Research*, *19*(1), 79–124.

Hernández-Guerra, A., Espino-Falcón, E., Vélez-Belchí, P., Pérez-Hernández, M. D., Martínez-Marrero, A., & Cana, L. (2017). Recirculation of the Canary Current in fall 2014. *Journal of Marine Systems*, *174*, 25–39.

Hernández-Guerra, A., Fraile-Nuez, E., López-Laatzen, F., Martínez, A., Parrilla, G., & Vélez-Belchí, P. (2005). Canary Current and North Equatorial Current from an inverse box model. *Journal of Geophysical Research: Oceans*, *110*(C12). https://doi.org/10.1029/2005JC003032.

Hernández-Guerra, A., & Talley, L. D. (2016). Meridional overturning transports at 30°S

in the Indian and Pacific Oceans in 2002–2003 and 2009. *Progress in Oceanography*, *146*, 89–120. https://doi.org/10.1016/j.pocean.2016.06.005.

Hernández-Guerra, A., Talley, L. D., Pelegrí, J. L., Vélez-Belchí, P., Baringer, M. O., Macdonald, A. M., & McDonagh, E. L. (2019). The upper, deep, abyssal and overturning circulation in the Atlantic Ocean at 30°S in 2003 and 2011. *Progress in Oceanography*, *176*, 102136. https://doi.org/10.1016/j.pocean.2019.102136.

Joyce, T. M., Hernández-Guerra, A., & Smethie, W. M. (2001). Zonal circulation in the NW Atlantic and Caribbean from a meridional World Ocean Circulation Experiment hydrographic section at 66 W. *Journal of Geophysical Research: Oceans*, *106*(C10), 22095–22113.

Kalnay, E., Kanamitsu, M., Kistler, R., Collins, W., Deaven, D., Gandin, L., Iredell, M., Saha, S., White, G., Woollen, J., Zhu, Y., Chelliah, M., Ebisuzaki, W., Higgins, W., Janowiak, J., Mo, K. C., Ropelewski, C., Wang, J., Leetmaa, A., Reynolds, R., Jenne, R., & Joseph, D. (1996). The NCEP/NCAR 40-Year Reanalysis Project. *Bulletin of the American Meteorological Society*, *77*(3), 437–471. https://doi.org/10.1175/1520-0477(1996)077<0437:TNYRP>2.0.CO;2.

Katsumata, K., & Fukasawa, M. (2011). Changes in meridional fluxes and water properties in the Southern Hemisphere subtropical oceans between 1992/1995 and 2003/2004. *Progress in Oceanography*, *89*(1–4), 61–91. https://doi.org/10.1016/j.pocean.2010.12.008.

Kawano, T., Fukasawa, M., Kouketsu, S., Uchida, H., Doi, T., Kaneko, I., Aoyama, M., & Schneider, W. (2006). Bottom water warming along the pathway of lower circumpolar deep water in the Pacific Ocean. *Geophysical Research Letters*, *33*. https://doi.org/10.1029/2006GL027933.

Knauss, J. A. (1962). On some aspects of the deep circulation of the Pacific. *Journal of Geophysical Research*, *67*(10), 3943–3954. https://doi.org/10.1029/JZ067i010p03943.

Lumpkin, R., & Speer, K. (2007). Global Ocean Meridional Overturning. *Journal of Physical Oceanography*, *37*(10), 2550–2562. https://doi.org/10.1175/JPO3130.1.

Macdonald, A. M. (1995). *Oceanic fluxes of mass, heat and freshwater*. *A global estimate and perspective*. (No. MIT/WHOI-95-25). MASSACHUSETTS INST OF TECH CAMBRIDGE.

Macdonald, A. M., Mecking, S., Robbins, P. E., Toole, J. M., Johnson, G. C., Talley, L., Cook, M., & Wijffels, S. E. (2009). The WOCE-era 3-D Pacific Ocean circulation and heat budget. *Progress in Oceanography*, *82*(4), 281–325. https://doi.org/10.1016/j.pocean.2009.08.002.

Macdonald, A. M., & Wunsch, C. (1996). An estimate of global ocean circulation and heat fluxes. *Nature*, *382*, 436–439.

Mata, M. M., Tomczak, M., Wijffels, S., & Church, J. A. (2000). East Australian Current volume transports at 30°S: Estimates from the World Ocean Circulation Experiment hydrographic sections PR11/P6 and the PCM3 current meter array. *Journal of Geophysical Research: Oceans*, *105*(C12), 28509–28526. https://doi.org/10.1029/1999jc000121.

McCarthy, M. C., Talley, L. D., & Roemmich, D. (2000). Seasonal to interannual variability from expendable bathythermograph and TOPEX/Poseidon altimeter data in the South Pacific subtropical gyre. *Journal of Geophysical Research: Oceans*, *105*(C8), 19535–19550.

Montes, I., Colas, F., Capet, X., & Schneider, W. (2010). On the pathways of the equatorial subsurface currents in the eastern equatorial Pacific and their contributions to the Peru-Chile Undercurrent. *Journal of Geophysical Research*, *115*(C9), C09003. https://doi.org/10.1029/2009JC005710.

Mulhearn, P. J. (1987). The Tasman Front: A study using satellite infrared imagery. *Journal of Physical Oceanography*, *17*(9), 1148–1155.

Neshyba, S. (1979). On the southernmost extension of the Peru-Chile Undercurrent. *Deep-Sea Research Part A. Oceanographic Research Papers*, *26*(12), 1387–1393.

Purkey, S. G., Johnson, G. C., Talley, L. D., Sloyan, B. M., Wijffels, S. E., Smethie, W., Mecking, S., & Katsumata, K. (2019). Unabated Bottom Water Warming and Freshening in the South Paci fi c Ocean Journal of Geophysical Research : Oceans. *Journal of Geophysical Research: Oceans*, *124*(3), 1778–1794. https://doi.org/10.1029/2018JC014775.

Reid, J. L. (1997). On the total geostrophic circulation of the pacific ocean: flow patterns, tracers, and transports. *Progress in Oceanography*, *39*(4), 263–352. https://doi.org/10.1016/S0079-6611(97)00012-8.

Ridgway, K. R., & Godfrey, J. S. (1994). Mass and heat budgets in the East Australian Current: A direct approach. *Journal of Geophysical Research: Oceans*, *99*(C2), 3231–3248.

Roemmich, D., & Cornuelle, B. (1992). The subtropical mode waters of the South Pacific Ocean. *Journal of Physical Oceanography*. https://doi.org/10.1175/1520-0485(1992)022<1178:TSMWOT>2.0.CO;2.

Roemmich, D., & Wunsch, C. (1985). Two transatlantic sections: meridional circulation and heat flux in the subtropical North Atlantic Ocean. *Deep Sea Research Part A. Oceanographic Research Papers*, *32*(6), 619–664. https://doi.org/10.1016/0198-0149(85)90070-6.

Schmitz, W. (1995). On the interbasin-scale thermohaline circulation. *Reviews of Geophysics*, *33*, 151–173.

Shaffer, G., Hormazabal, S., Pizarro, O., & Salinas, S. (1999). Seasonal and interannual variability of currents and temperature off central Chile. *Journal of Geophysical Research: Oceans*, *104*, 29951–29961.

Silva, N., Rojas, N., & Fedele, A. (2009). Water masses in the Humboldt Current System: Properties, distribution, and the nitrate deficit as a chemical water mass tracer for Equatorial Subsurface Water off Chile. *Deep-Sea Research*, *56*, 1004–1020. https://doi.org/10.1016/j.dsr2.2008.12.013.

Sprintall, J., & Tomczak, M. (1993). On the formation of Central Water and thermocline ventilation in the southern hemisphere. *Deep-Sea Research*, *I 40*, 827–848.

Sprintall, J., Wijffels, S. E., Molcard, R., & Jaya, I. (2009). Direct estimates of the Indonesian Throughflow entering the Indian Ocean: 2004–2006. *Journal of Geophysical Research: Oceans*, *114*(C7). https://doi.org/10.1029/2008JC005257.

Stanton, B. R. (1979). The Tasman Front. *New Zealand Journal of Marine Freshwater Research*, *13*(2), 201–214.

Stramma, L., Johnson, G. C., Firing, E., & Schmidtko, S. (2010). Eastern Pacific oxygen minimum zones: Supply paths and multidecadal changes. *Journal of Geophysical Research*, *115*(C9), C09011. https://doi.org/10.1029/2009JC005976.

Strub, P. T., Mesias, J. M., Montecino, V., Ruttlant, J., & Salinas, S. (1998). Coastal ocean circulation off western South America, in The Sea, vol. 11, The Global Coastal Ocean: Regional Studies and Syntheses, edited by A. R. Robinson & K. H. Brink, pp. 273-314, John Wiley, Hoboken, N. J.

Talley, L. D. (2003). Shallow, intermediate, and deep overturning components of the global heat budget. *Journal of Physical Oceanography*, *33(3)*, 530–560.

Talley, L. D. (2008). Freshwater transport estimates and the global overturning circulation: sallow, deep and throughflow components. *Progress in Oceanography*, *78*, 257–303.

Talley, L. D. (2013). Closure of the Global Overturning Circulation Through the Indian, Pacific, and Southern Oceans: Schematics and Transports. *Oceanography*, *26*(1), 80–97. https://doi.org/10.5670/oceanog.2013.07.

Talley, L. D., Feely, R. A., Sloyan, B. M., Wanninkhof, R., Baringer, M. O., Bullister, J. L., Carlson, C. A., Doney, S. C., Fine, R. A., Firing, E., Gruber, N., Hansell, D. A., Ishii, M., Johnson, G. C., Katsumata, K., Key, R. M., Kramp, M., Langdon, C., MacDonald, A. M., Mathis, J. T., McDonagh, E. L., Mecking, S., Millero, F. J., Mordy, C. W.., Nakano, T., Sabine, C. L., Smethie, W. M., Swift, J. H., Tanhua, T., Thurnherr, A. M., Warner, M. J., & Zhang, J. Z. (2016). Changes in Ocean Heat, Carbon Content, and

Ventilation: A Review of the First Decade of GO-SHIP Global Repeat Hydrography. *Annual Review of Marine Science*, *8*(1), 185–215. https://doi.org/10.1146/annurev-marine-052915-100829.

Talley, L. D., Pickard, G. L., Emery, W. J., & Swift, J. H. (2011). *Descriptive Physical Oceanography: An Introduction* (Sixth). B: Elsevier Ltd.

Talley, L. D., Reid, J. L., & Robbins, P. E. (2003). Data-based meridional overturning streamfunctions for the global ocean. *Journal of Climate*, *16*(19), 3213–3226.

Talley, L. D., & Sprintall, J. (2005). Deep expression of the Indonesian Throughflow: Indonesian intermediate water in the South Equatorial Current. *Journal of Geophysical Research: Oceans*, *110*(C10).

Tilburg, C. E., Hurlburt, H. E., O'Brien, J. J., & Shriver, J. F. (2001). The Dynamics of the East Australian Current System: The Tasman Front, the East Auckland Current, and the East Cape Current. *Journal of Physical Oceanography*, *31*(10), 2917–2943. https://doi.org/10.1175/1520-0485(2001)031<2917:TDOTEA>2.0.CO;2.

Tomczak, M., & Godfrey, J. S. (1994). *Regional oceanography: an introduction*. Pergamon, Tarrytown, N. Y.

Tsimplis, M. N., Bacon, S., & Bryden, H. L. (1998). The circulation of the subtropical South Pacific derived from hydrographic data. *Journal of Geophysical Research: Oceans*, *103*(C10), 21443–21468.

Tsuchiya, M. (1990). Flow path of the Antarctic Intermediate Water in the western equatorial South Pacific Ocean. *Deep-Sea Research*, *33*, S273–S279. https://doi.org/10.1016/S0198-0149(12)80013-6.

Tsuchiya, M., & Talley, L. D. (1996). Water-property distributions along an eastern Pacific hydrographie section at 135W. *Journal of Marine Research*, *54*(3), 541–564. https://doi.org/10.1357/0022240963213583.

Tsuchiya, M., & Talley, L. D. (1998). A Pacific hydrographic section at 88°W: Water-property distribution. *Journal of Geophysical Research*, *103*(C6), 12899–12918.

Vélez-Belchí, P., Pérez-Hernández, M. D., Casanova-Masjoan, M., Cana, L., & Hernández-Guerra, A. (2017). On the seasonal variability of the Canary Current and the Atlantic Meridional Overturning Circulation. *Journal of Geophysical Research: Oceans*, *122*(6), 4518–4538.

Whitworth, T., Warren, B. A., Nowlin Jr, W. D., Rutz, S. B., Pillsbury, R. D., & Moore, M. I. (1999). On the deep western-boundary current in the Southwest Pacific Basin. *Progress in Oceanography*, *43*(1), 1–54.

Wijffels, S. E., Hall, M. M., Joyce, T., Torres, D. J., Hacker, P., & Firing, E. (1998). Multiple deep gyres of the western North Pacific: A WOCE section along 149°E. *Journal of Geophysical Research: Oceans*, *103*(C6), 12985–13009. https://doi.org/10.1029/98JC01016.

Wijffels, S. E., Toole, J. M., & Davis, R. (2001). Revisiting the South Pacific subtropical circulation: A synthesis of World Ocean Circulation Experiment observations along 32°S. *Journal of Geophysical Research: Oceans*, *106*(C9), 19481–19513. https://doi.org/10.1029/1999jc000118.

Wooster, W. S., & Gilmartin, M. (1961). The Peru-Chile Undercurrent. *Journal of Marine Research*, *19*, 97–122.

Wooster, W. S., & Reid, J. L. (1963). Eastern boundary currents. *The Sea, Ideas and Observations on Progress in the Study of the Seas*, *2*, 253–280.

Wunsch, C. (1977). Determining the general circulation of the oceans: a preliminary discussion. *Science*, *196*, 871–875.

Wunsch, C. (1978). North-Atlantic general circulation west of 50°W determined by inverse methods. *Reviews of Geophysics*, *16*, 583–620.

Wunsch, C. (1996). *The Ocean Circulation Inverse Problem*. Cambridge University Press.

Wunsch, C., Hu, D., & Grant, B. (1983). Mass, heat, salt and nutrient fluxes in the South Pacific Ocean. *Journal of Physical Oceanography*, *13*(5), 725–753.

Wyrtki, K. (1967). Circulation and water masses in the Eastern Equatorial Pacific Ocean. *Int. J. Oceanol. & Limnol*, *1*, 117–147.

Wyrtki, K. (1975). Fluctuations of the Dynamic Topography in the Pacific Ocean. *Journal of Physical Oceanography*, *5*(3), 450–459. https://doi.org/10.1175/1520-0485(1975)005<0450:FOTDTI>2.0.CO;2.